Contrat CNES Année 2021

*BC : **4500070532 / DSO091***

Note technique sur l'amélioration du cycle des poussières dans le GCM

Ref : LMD_CNES_EXM_2021_dust_cycle

Préparé par : Antoine Bierjon, François Forget, Ehouarn Millour

Laboratoire de Météorologie Dynamique, CNRS, IPSL, Paris, France.

30 décembre 2021

Contents

Introduction

This document reviews the improvements concerning the modelling of the dust cycle in the Martian Global Climate Model version 6 and the related work that has been carried throughout the year 2021.

This work strongly relies upon the studies and developments that have been detailed in the previous reports addressing the LMD Mars GCM dust cycle, namely *LMD_CNES_EXM_gcm6.0* (2019) and *LMD_CNES_EXM_2020_gcm_dust*.

The first one introduced the core processes of our new GCM6 dust cycle : the new dust injection, driven by the column-integrated optical depth scenarios, let the dust evolve more freely accordingly to the weather processes, and to avoid nonphysical renormalization ; the *rocket dust storms* are activated by the sun radiation that heats pockets of concentrated aerosols during the dusty season and makes them soar to high altitudes ; and the *mountain top flows* (previously named *slope winds*), triggered all year long by midday updraft winds over converging slopes, entrain near surface dust toward the orographic summits and above.

Last year, the validation of these parametrizations was studied thanks to a refined comparison to the observations from the *Mars Climate Sounder* (Kleinböhl et al. [2009], Montabone et al. [2017]) onboard Mars Reconnaissance Orbiter, as well as a tuning campaign to better constrain the free parameters of the GCM dust cycle. Despite encouraging results, this scrutiny emphasized some model misconceptions and persisting biases, that we aimed to fix over this year.

In **Section 1**, we apply a correction to the *mountain top flows* scheme, that limits the activation of the process only to the main "converging slopes" - mountains - present at the Martian surface. The former version of the code was indeed generalized to every grid meshes assuming that their characteristic orography corresponded to converging slopes, thus introducing strong reinjection of dust in the atmosphere around regions like Hellas Planitia or Valles Marineris, which was not compliant with the scenarios.

Section 2 presents our work around the discrepancy between the respective evaluations of the model with regard to the visible/near-IR Column-integrated Dust Optical Depth scenarios from Montabone et al. [2015], and to the 21.6µm dust opacity retrievals from *MCS*. Since the dust opacity is a major component of the radiative transfer in the Martian atmosphere, we explore the consequence of our findings on solving the atmospheric temperature hot bias identified in the GCM6 in the previous report.

Finally, **Section 3** quickly explains the choice we made to widen the dust injection timing to the whole 24h sol in the model.

These changes in the model enabled us to simulate a dust cycle that is closer to the observations, as detailed in **Section 4**, and upon which the version 6.1 of the *Mars Climate Database* should be produced in the near future.

1 Mountain top flows scheme

This section tackles the changes we performed in the mountain top flows parametrization (referred as *slope winds* in preceding reports), in order to make it more realistic and in line with the original idea behind it. In fact, the former scheme used to assign to every surface mesh grid a characteristic height h_{mons} that was computed from the local orography and that activated the top flows scheme on a subgrid mesh fraction :

$$x_{mons} = C_{mons} \frac{h_{mons} - h_{min}}{h_{max} - h_{min}} \tag{1}$$

with h_{min} and h_{max} respectively the lowest and highest value of h_{mons} all around the globe, and C_{mons} a tunable coefficient. The Figure 1 illustrates the spatial variation of h_{mons} in the GCM.

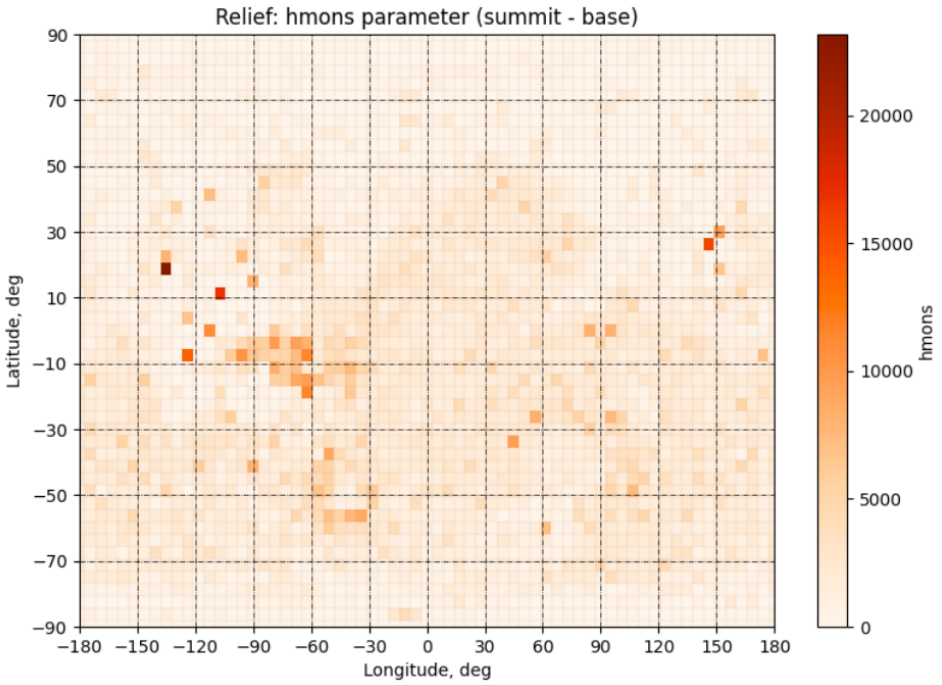

Figure 1: Registered GCM characteristic height h_{mons} for a 64x48 horizontal resolution, computed from MOLA datum as detailed in *LMD_CNES_EXM_gcm6.0*.

We could then weight the efficiency of the top flows accordingly to the mesh fraction, as described in *LMD_CNES_EXM_gcm6.0* : if x_{mons} is large, a greater quantity of *topdust* will be reinjected from the boundary layer, but it will also be less concentrated as far as the radiative transfer is concerned, as the whole process operates in this fixed fraction. This simple method has some flaws however.

As the *topdust* is a tracer in the model, it can be transported from the column it originated from (for instance, one with a big mountain like Olympus Mons) to adjacent meshes with flatter topography. Since each mesh has its own x_{mons}, and as the GCM tracers have no memory of their origin, the huge amount of quite spread *topdust* created in this Olympus Mons fraction could cross the mesh boundaries, hence arriving in a mesh with a smaller x_{mons} that artificially makes it more concentrated than it was before. This concentrated *topdust* generates a stronger local radiative heating that carries it to higher altitudes than what it would have reached normally.

Besides, this scheme proved to be overgeneralizing, as it mixes up very distinct kinds of topography that may not have the accounted effect of concentrating dust above their summits. This is particularly true for cliff landscapes, which exhibit some steep and extended elevations, but do not present the effect due to the converging aspect of a mountain's slopes. Hence, with the former parametrization, the model resulted in strong dust reinjection in places like the canyon of Valles Marineris, or the impact bassins of Hellas and Argyre Planitia. They were for instance responsible for an opaque feature in the clear season around 10-30°S when looking at the Column-integrated Dust Optical Depth (*CDOD*) maps, which didn't correspond to the scenarios used to force the dust injection (see Figure 2).

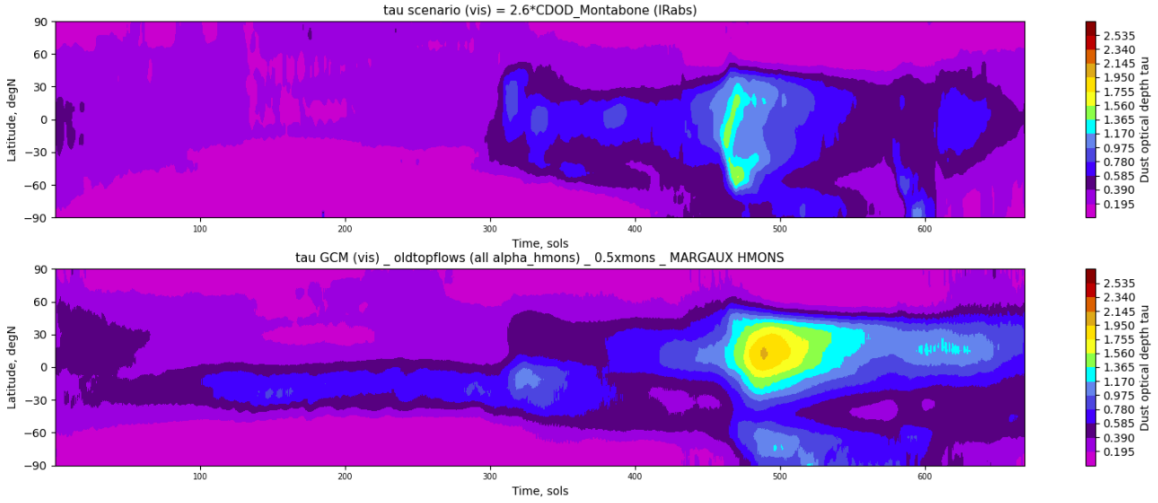

Figure 2: Time[sols]-latitude[°N] evolution maps over MY29 of **Top:** visible $\tau_{scenario}$ from Montabone et al. [2015] **Bottom:** visible τ_{GCM}, with the old top flows scheme. Every integrated optical depths are normalized to a pressure of 610Pa.

These unrealistic behaviours led us to refine the mountain top flows so that they represent well what they were originally designed for.

Revisiting this scheme began by making an inventory of the major known converging slopes on the surface of Mars. To that end, the Mars Trek portal developed by NASA JPL (Law and Day [2017]) was of great help as a way to confirm the presence of mountains. We listed a total of 19 topographic features, among which the five great volcanoes (Olympus, the three from Tharsis region and Elysium Mons) and smaller ones, but also geological massifs like Anseris Mons (Hellas Planitia) or Aeolis Mons (Gale crater). This list, non-exhaustive but still comprising the main converging slopes of the Martian surface, is detailed in Table 1 below. We chose to keep the characteristic height that was given to the grid meshes containing these mountains in the former scheme, and put all the other h_{mons} to zero, preventing the top flows to activate there. We can note that this also implies detraining the *topdust* into background dust as soon as it leaves the columns containing mountains, which may not be that realistic either but still seems a better solution.

Since we restrict the top flows scheme to these mountains only, we decide not to dampen their effect too much by keeping the fraction x_{mons} as a linear function of h_{mons}, with a C_{mons} coefficient of 0.5.

These changes in the modelling of mountain top flows result in a much more reasonable optical depth, as can be seen on Figure 3. On the dust vertical profile, highlighted by

Mountain name	**Location (longitude ; latitude)**	**GCM mesh h_{mons} (summit-base)**
Olympus Mons	-134.0°E ; 18.4°N	23.2km
Ascraeus Mons	-104.5°E ; 11.8°N	16.8km
Elysium Mons	146.9°E ; 24.8°N	15.9km
Arsia Mons	-121.1°E ; -8.4°N	14.0km
Pavonis Mons	-113.4°E ; -0.8°N	11.1km
Hecates Tholus	150.2°E ; 31.8°N	9.4km
Tharsis Tholus	-90.8°E ; 13.4°N	8.0km
Ceraunius Tholus	-97.4°E ; 24.0°N	7.4km
Alba Mons	-109.6°E ; 40.4°N	7.2km
Apollinaris Mons	174.4°E ; 18.4°N	7.0km
Albor Tholus	150.4°E ; 18.8°N	6.6km
Biblis Tholus	-124.6°E ; 2.6°N	6.6km
Anseris Mons	86.6°E ; -29.8°N	5.6km
Ulysses Tholus	-121.6°E ; 2.9°N	6.6km *(merged with Biblis Tholus in the 64x48 GCM resolution)*
Aeolis Mons	137.8°E ; -5.4°N	4.3km
Euripus Mons	105.0°E ; -44.8°N	4.1km
Hadriacus Mons	91.8°E ; -32.1°N	2.4km
Tyrrhenus Mons	106.5°E ; -21.1°N	1.5km
Uranius Mons	-92.2°E ; 26.8°N	1.5km

Table 1: List of inventoried mountains in the GCM new top flows scheme, and the h_{mons} parameter of their corresponding grid mesh in the usual 64x48 horizontal resolution.

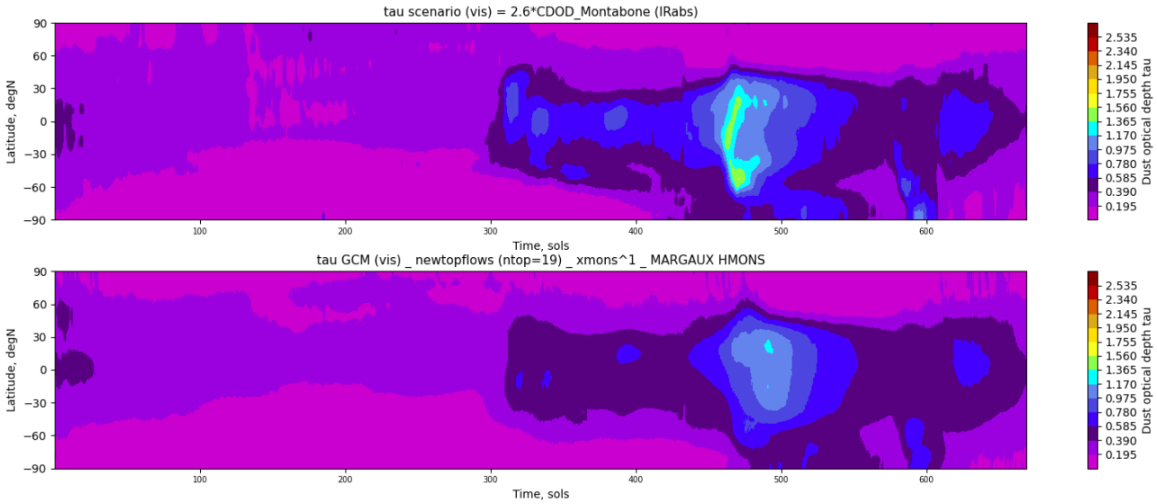

Figure 3: Time[sols]-latitude[°N] evolution maps over MY29 of **Top:** visible $\tau_{scenario}$ (fixed 2.6 IR to VIS coefficient) **Bottom:** visible τ_{GCM}, with the new top flows scheme. Every integrated optical depths are normalized to a pressure of 610Pa.

Figure 4, the detached layers present before are now shallower in the clear season, even compared to *MCS*, but the new top flows still enable some dust to reach mid altitudes (pressures below 100Pa). In the second half of the year, the effect of the changes are less pronounced because of the prominence of the rocket dust storms, apart from the period after Ls 300° that sees a strong decrease in amplitude (but not in altitude) of the detached

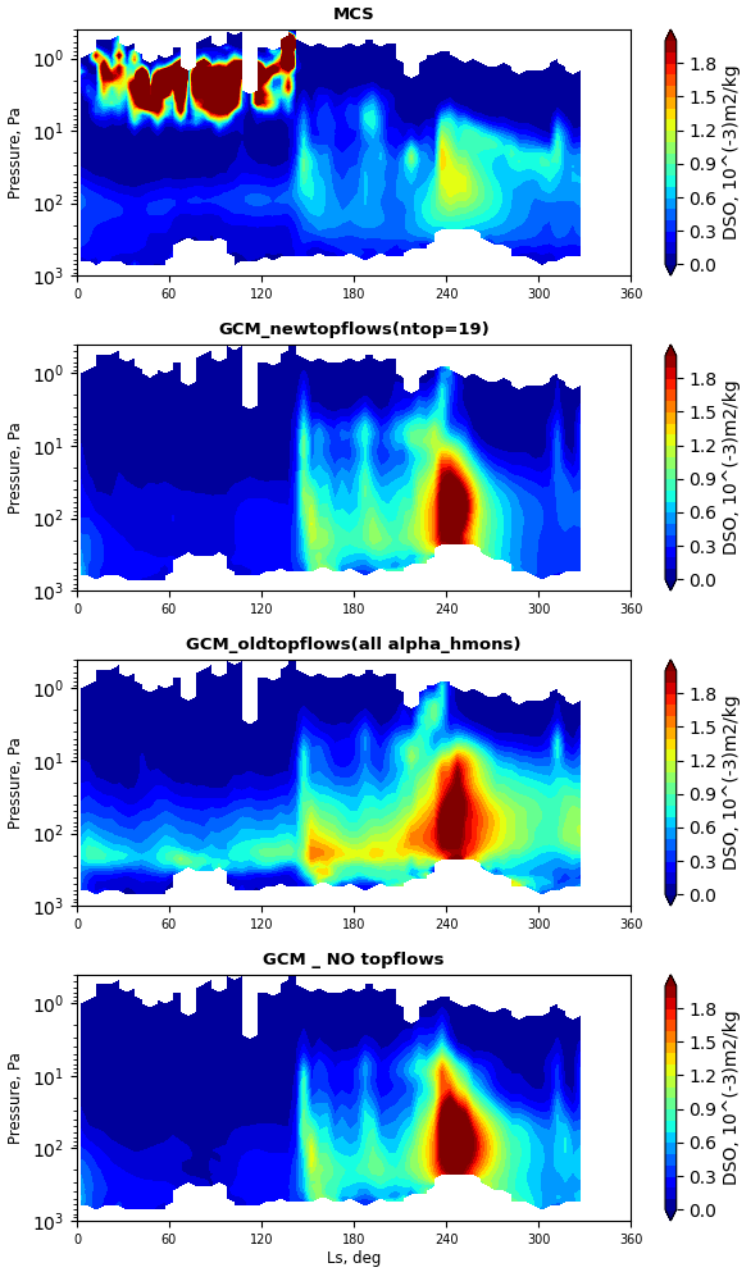

Figure 4: Nighttime dust Density-Scaled Opacity at 21.6µm from *MCS* and several GCM simulations - Zonal & meridional average in latitude band of [30°S;30°N] - MY29. **Top to bottom:** *MCS* ; GCM6 with new top flows scheme ; GCM6 with old top flows scheme ; GCM6 without top flows.

layers, even compared to the simulation without top flows. Eventually, the strong peak in density-scaled opacity is still present around Ls 240°, as the discrepancy between *MCS* observations and the CDOD visible scenarios stands out here, after having been longly exposed in the previous report *LMD_CNES_EXM_2020_gcm_dust*. In the next section, we look for a way out of this paradox, by trying out different changes concerning the optical properties of the dust aerosol.

2 Optical properties and comparison to observations

As mentioned in Section 1 and explained in the previous reports, in order to simulate a realistic Martian dust cycle, the GCM is forced by Column-integrated Dust Optical Depth (*CDOD*) scenarios. These scenarios have been built by Montabone et al. [2015] based on the observations from multiple instruments orbiting the planet. The major supply of opacity measurements used in the latest Martian Years is from *Mars Climate Sounder*, a mid- and far-infrared thermal emission radiometer performing nadir and limb soundings of the atmosphere (Kleinböhl et al. [2009]). This instrument measures dust absorption opacity profiles at the IR wavelength of 21.6µm, which is then converted into extinction opacity in the retrievals thanks to the relation $\tau_{ext} = \frac{\tau_{abs}}{(1-\omega)}$. ω represents the single scattering albedo of the dust particle, assumed to be 0.0550 by Kleinböhl et al. [2011].

To build the CDOD scenarios, these extinction opacity profiles at 21.6µm are then extrapolated down to the surface, and Montabone et al. infer an IR absorption optical depth at 9.3µm using a ratio of 2.7 from the opacity at 21.6µm.

Finally, in the model, we compute a visible (0.67µm) extinction CDOD from the absorption 9.3µm scenario using a coefficient of 2.6 mentioned in Montabone et al. [2015], and we make the model visible CDOD follow the scenario by injecting each day a dust amount corresponding to the difference between the two. Using these hypotheses, we found that the model exhibits paradoxical behaviours, as the visible CDOD remains near below the target scenario, while the comparison to the direct *MCS* 21.6µm extinction opacity suggests a strong overestimation of the modeled atmospheric dust quantity.

In the *LMD_CNES_EXM_2020_gcm_dust* report that demonstrated this discrepancy, we concluded with two perspectives to try to reconcile these validation datasets. This is what we explore in this section.

2.1 Optical properties and conversion between opacities

As explained before, the transition from the *MCS* measurements in the mid-far infrared to the visible CDOD scenario as it is used in the GCM requires to go through two conversions, which carry some hypotheses on the particle distribution.

The size of the dust particles present in the atmosphere is assumed to follow a log-normal distribution, that can be fully described by the tuple of its effective radius r_{eff} and variance ν_{eff}.

For the dust scenarios, the 2.7 coefficient in Montabone's article, used to do the conversion $\tau_{ext,21.6\mu m} \rightarrow \tau_{abs,9.3\mu m}$, supposes a r_{eff}=1.06µm and ν_{eff}=0.3. If we look at the theoretical conversion coefficient to apply, this corresponds to :

$$\frac{\tau_{abs,9.3\mu m}}{\tau_{ext,21.6\mu m}} = \frac{Q_{ext,9.3\mu m} * (1 - \omega_{9.3\mu m})}{Q_{ext,21.6\mu m}} \tag{2}$$

with τ_{ext} the extinction opacities [1/km]. The extinction efficiencies Q_{ext} and the single scattering albedo ω are the optical properties of the dust particles, which depend on the size distribution. In the GCM, we use tabulated optical properties computed from a T-Matrix code for a large range of effective radii, at a very small variance that is almost representative of one isolated particle's optical properties. We can then compute the properties for multiple variances by convolution methods and simulate different size distributions.

On Figure 5, we plot the computed value of this theoretical coefficient for multiple variance assumptions, as well as the value and its error bar given by Montabone et al. [2015]. This shows that the coefficient value used to build the scenarios lies at the verge of a strong curve inflexion, with the theoretical value rapidly decreasing as r_{eff} increases. We can thus question the reliability of the 2.7 value to apprehend the dust distribution at every time of the year, everywhere around the globe. Especially, for a dust effective size shifted

towards 2µm, the scenarios would exhibit a 9.3µm optical depth almost twice higher than what the properties tables suggest.

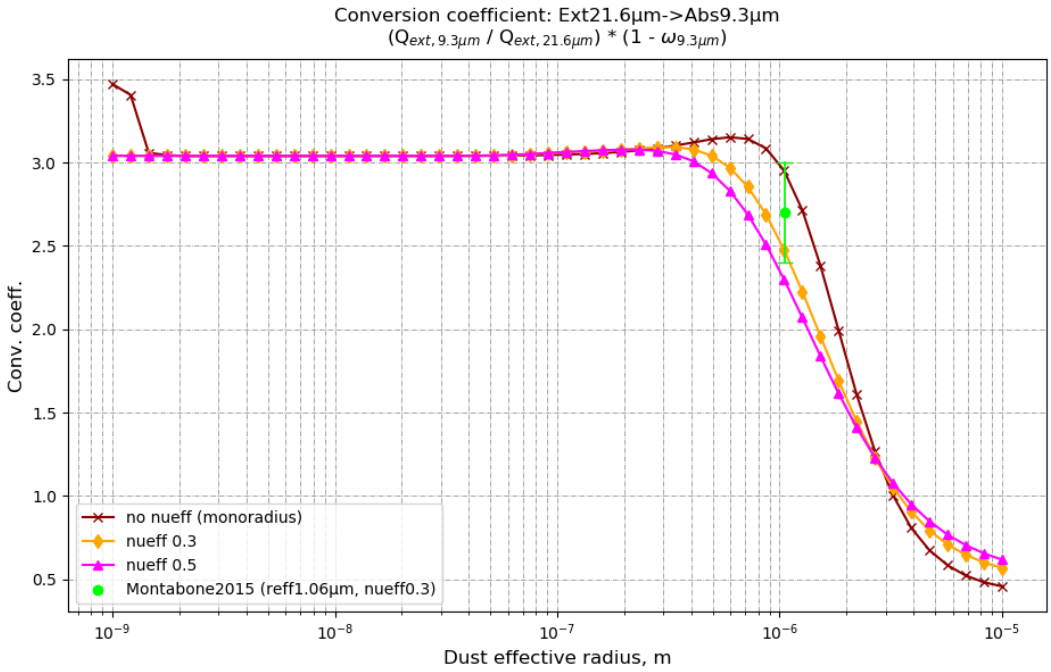

Figure 5: Conversion coefficient from dust extinction at 21.6µm to absorption at 9.3µm as a function of effective radius, computed from T-matrix generated tables of optical properties used in the GCM. The brown curve is computed with no dust distribution variance (isolated particles properties), the yellow and pink ones with ν_{eff} = 0.3 and 0.5 respectively. The green point and error bars are values reported from Montabone et al. [2015].

Nonetheless, Montabone et al. [2015] demonstrated a certain agreement between the scenarios derived from *MCS* and from the other instruments already calibrated at 9.3µm. This may be due to the fact that the *MCS* team makes a compensating error on their albedo of 0.0550 when computing extinction at 21.6µm from the observed absorption. For now, we decided to leave this question open, and we focused our actions on the second conversion coefficient.

For the conversion $\tau_{abs,9.3\mu m} \rightarrow \tau_{ext,0.67\mu m}$, Montabone et al. [2015] suppose a r_{eff}= 1.5-2µm which gives them a coefficient of 2.6. This corresponds in theory to the expression:

$$\frac{\tau_{ext,0.67\mu m}}{\tau_{abs,9.3\mu m}} = \frac{Q_{ext,0.67\mu m}}{Q_{ext,9.3\mu m} * (1 - \omega_{9.3\mu m})} \tag{3}$$

By doing the same plot than before for this coefficient on Figure 6, we can see an even stronger dependence on r_{eff}.

In the model, we work at a fixed dust effective variance of 0.5, while the effective radius in a grid mesh is given by the two transported dust moments, the mass mixing ratio q [kg_{dust}/kg_{air}] and the number mixing ratio N [$1/kg_{air}$]. Hence, we decided to implement a refined conversion of the 9.3µm absorption CDOD scenarios into visible extinction by taking into account the modeled r_{eff}. This is done while loading the scenario once per sol, as we compute the *IR to VIS ratio* as the ratio of the model CDOD at both wavelengths.

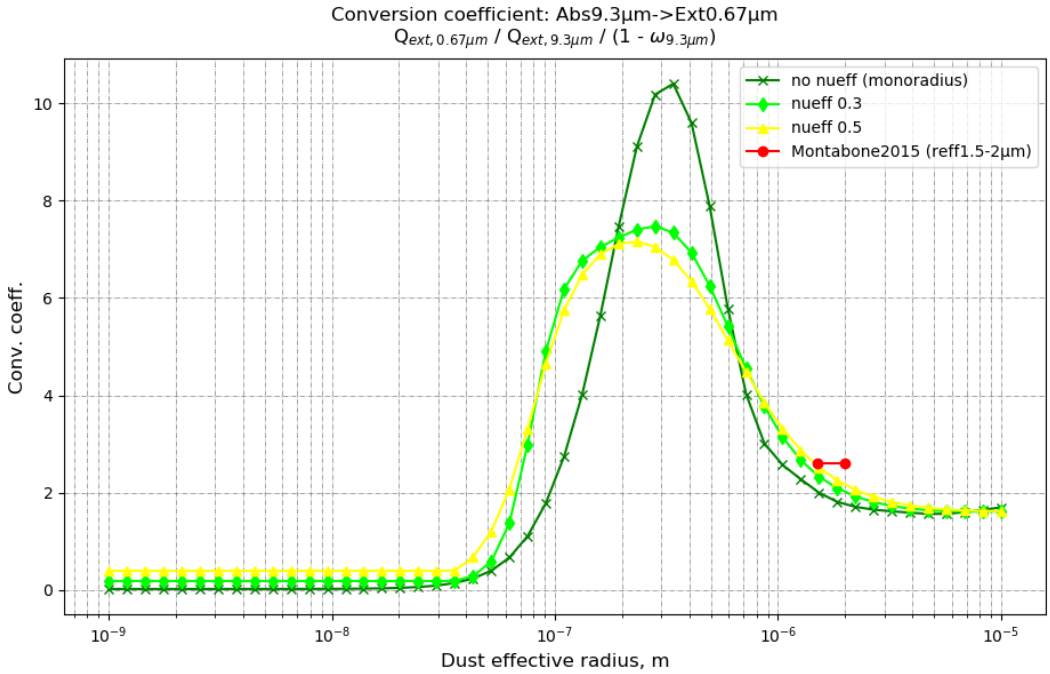

Figure 6: Conversion coefficient from dust absorption at 9.3µm to extinction at 0.67µm as a function of effective radius, computed from T-matrix generated tables of optical properties used in the GCM. The dark green curve is computed with no dust distribution variance (isolated particles properties), the lime green and yellow ones with ν_{eff} = 0.3 and 0.5 respectively. The red points are values reported from Montabone et al. [2015].

By analysing the evolution of this ratio on Figure 7 while keeping Figure 6 in mind, one can observe a net difference between the clear season, where only fine dust grains (approx. 1µm) stay in the atmosphere leading to an increased IR to VIS ratio, and the dusty season when the storms can lift larger particles (approx. 2µm), which deviate the dust size distribution towards lower conversion coefficients than before. In the polar nights finally, the coefficient follows Figure 6 as we go poleward, witnessing a decreasing particle size in these regions and times.

Therefore, it appears that taking into account this diversity of dust sizes in the conversion coefficient for the scenario results in a lower forcing during the second half of the year, making the GCM inject less dust than before (Figure 8) and get closer to *MCS* opacity profiles (Figure 9). On the other hand, by increasing the forcing in the first part of the year, it favors the persistence of mid-altitude (approx. 100Pa, or 20-30km) dust that can form *dust detached layers*.

On temperature aspect, as said before, the dust opacity plays a big role on the atmospheric thermal structure, via the radiative transfer. By decreasing the amount of dust injected during the dusty season, the varying IR to VIS ratio also has the effect of reducing the hot bias present in the model at this time, down by 5K in some cases (around Ls 240°,100Pa), as shown on Figure 10.

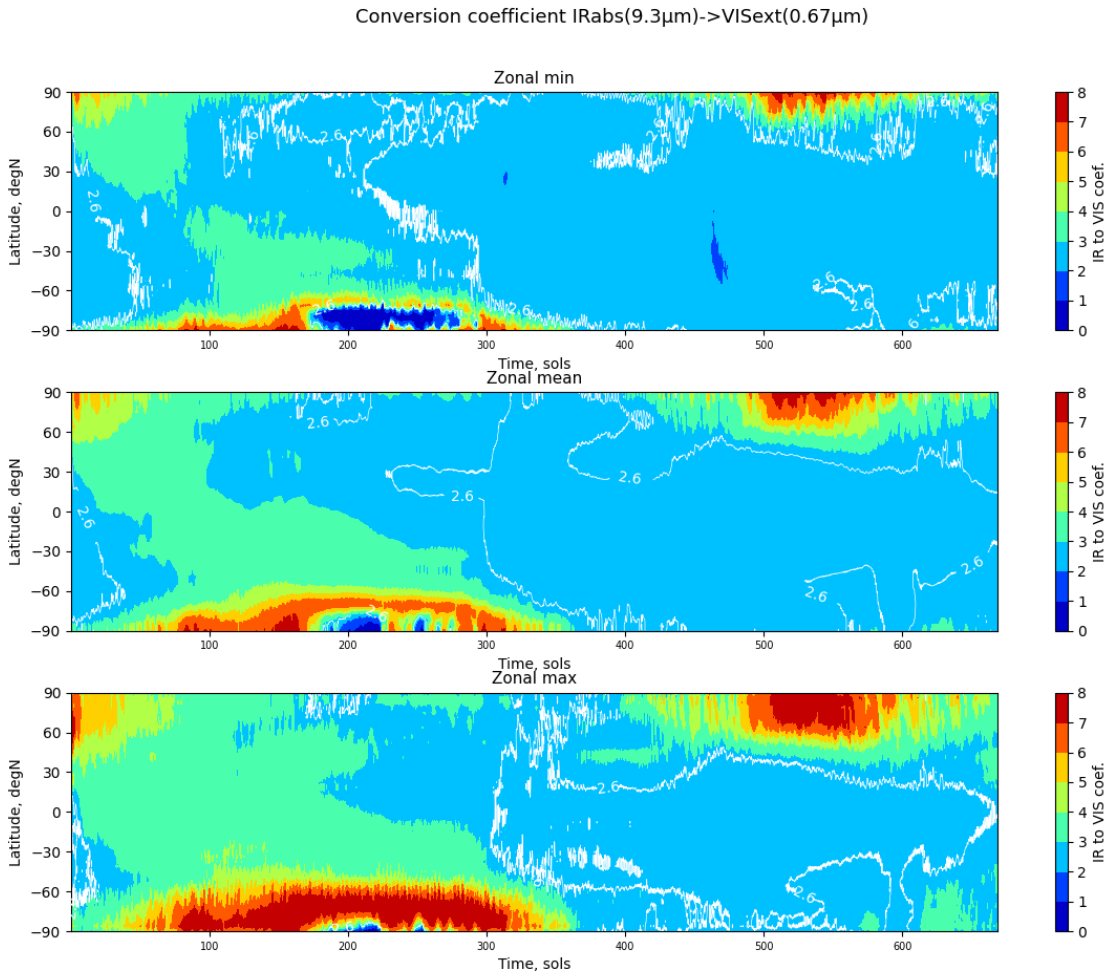

Figure 7: Evolution maps (time-latitude) of the computed IR to VIS ratio in the GCM over MY29. **Top:** zonal minimum. **Middle:** zonal average. **Bottom:** zonal maximum. The white contours delimit the plot areas above and below the former constant value of 2.6.

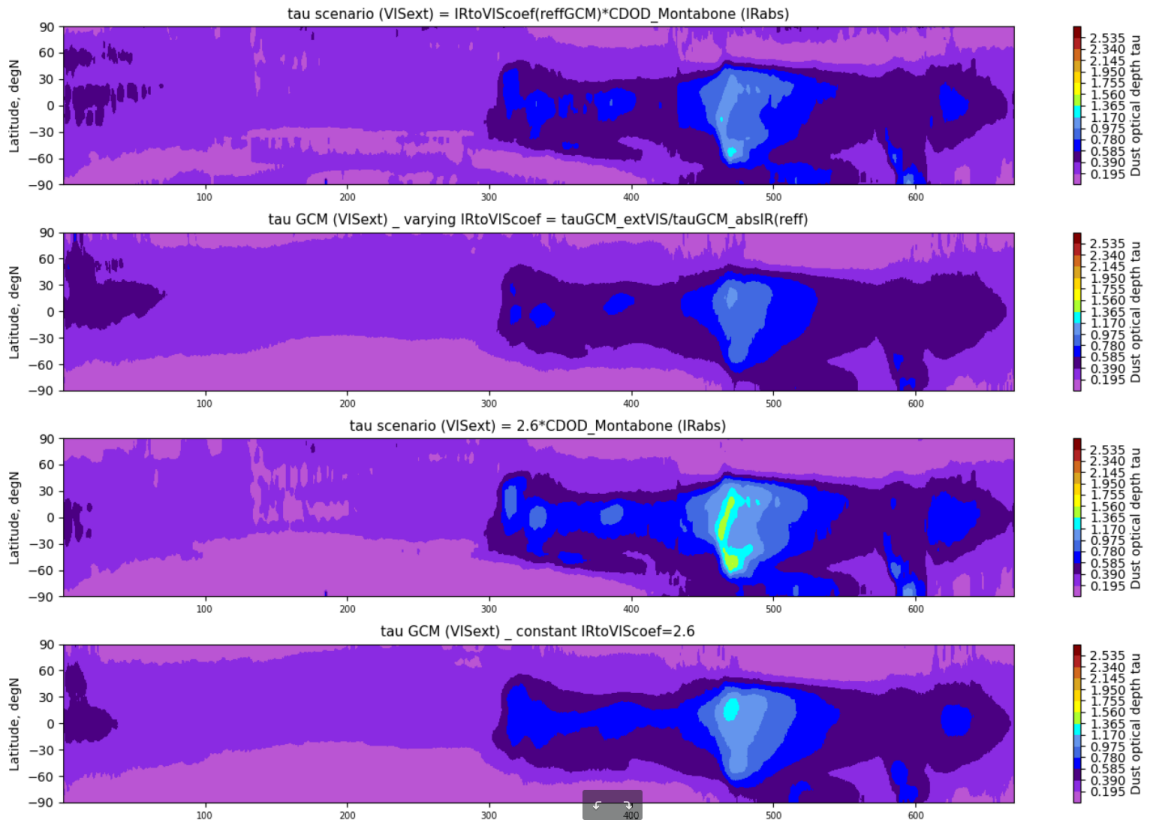

Figure 8: Time[sols]-latitude[°N] evolution maps over MY29 of visible $\tau_{scenario}$ and τ_{GCM} with and without IR to VIS ratio in the GCM. **Top 2 plots:** The visible CDOD scenario forcing, computed from IR (9.3µm absorption) scenario and the varying IR to VIS coefficient, and the correspondingly driven visible CDOD from the GCM. **Bottom 2 plots:** same plots as above but with the former constant value of 2.6. Every integrated optical depths are normalized to a pressure of 610Pa.

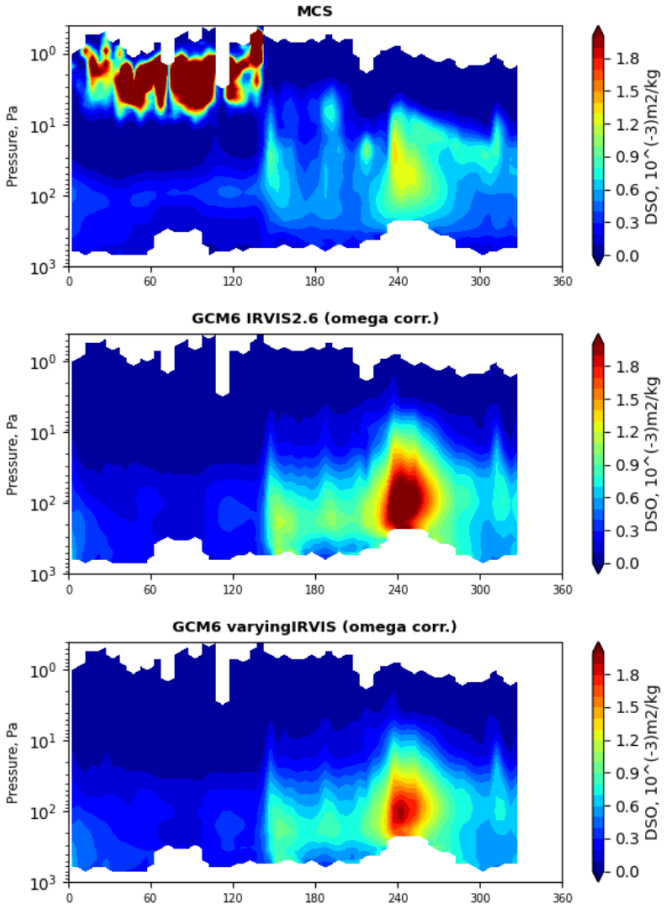

Figure 9: Nighttime dust Density-Scaled Opacity at 21.6µm from *MCS* and several GCM simulations - Zonal & meridional average in latitude band of [30°S;30°N] - MY29. **Top to bottom:** *MCS* ; GCM6 with constant 2.6 conversion coefficient for the scenario ; GCM6 with the new r_{eff}-dependent conversion coefficient for the scenario.

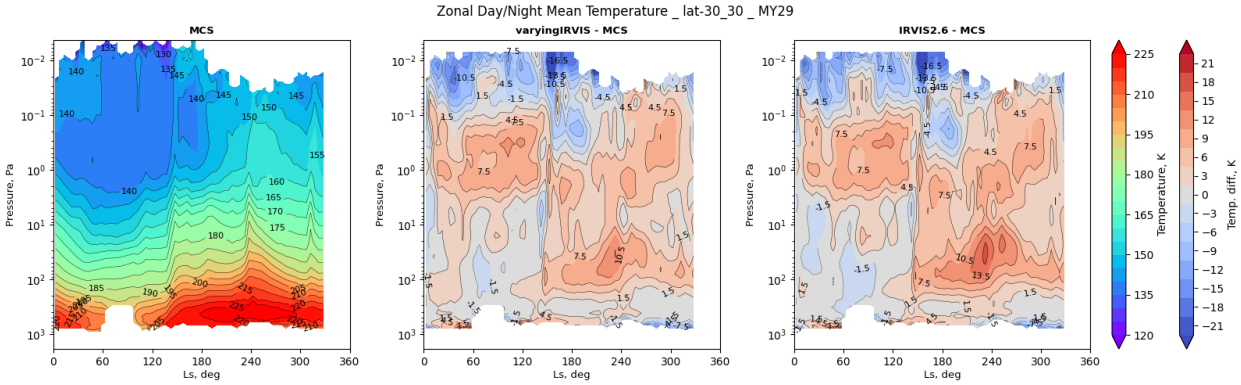

Figure 10: Diurnal mean temperature from *MCS* and GCM simulations - Zonal & meridional average in latitude band of [30°S;30°N] - MY29. **Left to right:** *MCS* absolute temperature ; Temperature difference between GCM6 with the new r_{eff}-dependent conversion coefficient and *MCS* ; Temperature difference between GCM6 with constant 2.6 conversion coefficient and *MCS*.

2.2 Constraining the GCM dust effective radius

Another possible cause of the discrepancy between GCM agreements to visible scenarios and *MCS* opacities could also be an unrealistic modeled dust size distribution. To be more precise, as we saw above, the dust optical properties tends to be particularly sensitive to the effective radius r_{eff}, especially at visible/near-IR wavelengths that are close to the particle characteristic size. It is thus critical to ensure that the model predicts accurate particle distributions. This validation of r_{eff} is even more needed now that the varying IR to VIS ratio we implemented increased the GCM sensitivity to the dust size.

This led us to look for observational datasets in order to better constrain the effective radius. On the one hand, we used the solar occultations data from Luginin et al. [2020], measured by the *Atmospheric Chemistry Suite* instrument onboard the Trace Gas Orbiter during the Mars Year 34. This dataset contains occultation profiles at morning and evening terminators between Ls 170.2° and 255.1°, with information on dust mass loading [g_{dust}/cm^3_{air}] and dust effective radius [µm]. We disregarded the specific conditions of the Global Dust Storm (GDS) that happened during this observed period, and focused on profiles before Ls 195° and after 240°, with a particular attention to the tropics. We compared these profiles with multiple MY29 GCM simulations, representative of a climatological year, in which we changed the effective radius $r_{eff,lift}$ of the dust when it is injected in the atmosphere, to values of 2, 2.5 and 3 microns (default value). Since processes like grain coagulation are not represented in the model, once the dust is injected with a given size distribution, the effective radius of this population is likely to decrease, especially due to mixing and sedimentation, and never reach back the $r_{eff,lift}$ value. Several points are to be noticed about the Figure 11 that presents these comparisons.

First of all, below 10km, the low number of ACS profiles makes it difficult to draw clear conclusions. This can be prejudicial for our validation, since the lower atmospheric layers generally account for the majority of the column-integrated optical depth. In spite of this, one can have the feeling of a peaked distribution between 10 and 20km, similar to the GCM, which could correspond to *dust detached layers*.

Moreover, the ACS profiles exhibit a strong vertical variability that contrast with the more homogeneous behaviour of the GCM r_{eff}. The difference in vertical resolution (1.6 GCM level per km in average between 5 and 60km, while some ACS profiles can contain more than 1 point every 500m) may be a reason for this, but should not be enough.

Comparing the GCM simulations together, one can observe a flattening of the mean profile with the decreasing $r_{eff,lift}$, and particularly a less pronounced peak between 10 and 20km. Indeed, larger particles are less opaque in visible than small ones, hence requiring more dust to be injected to follow the visible scenario forcing. However, the dependence on r_{eff} of the scenario discussed above, as well as the discriminating impact of the sedimentation onto different sizes may mitigate this effect.

But above all, these comparisons enlighten a strong model bias toward larger size distributions when running with the default $r_{eff,lift}$ = 3µm, that can be dampened by reducing the injected dust radius value.

On the other hand, we completed our validation thanks to a compilation of Curiosity ground measurements by Lemmon et al. [2019], who computed a dust effective radius on the atmospheric column seen by the rover over the years (see Figure 12). We compare this "column-integrated effective radius" to the GCM r_{eff} interpolated at Curiosity site and for different altitudes in the GCM column.

For an injection radius of 2.5 microns, which corresponds to Figure 13, we get an atmospheric dust r_{eff} that is compliant with the retrievals of climatological years from Lemmon et al. [2019]. Especially, the dust size almost never exceeds 2.0µm in the observations (apart from MY34 during the GDS), which is well represented in the displayed GCM run, but couldn't be achieved with the former higher $r_{eff,lift}$. Conversely, and as explained

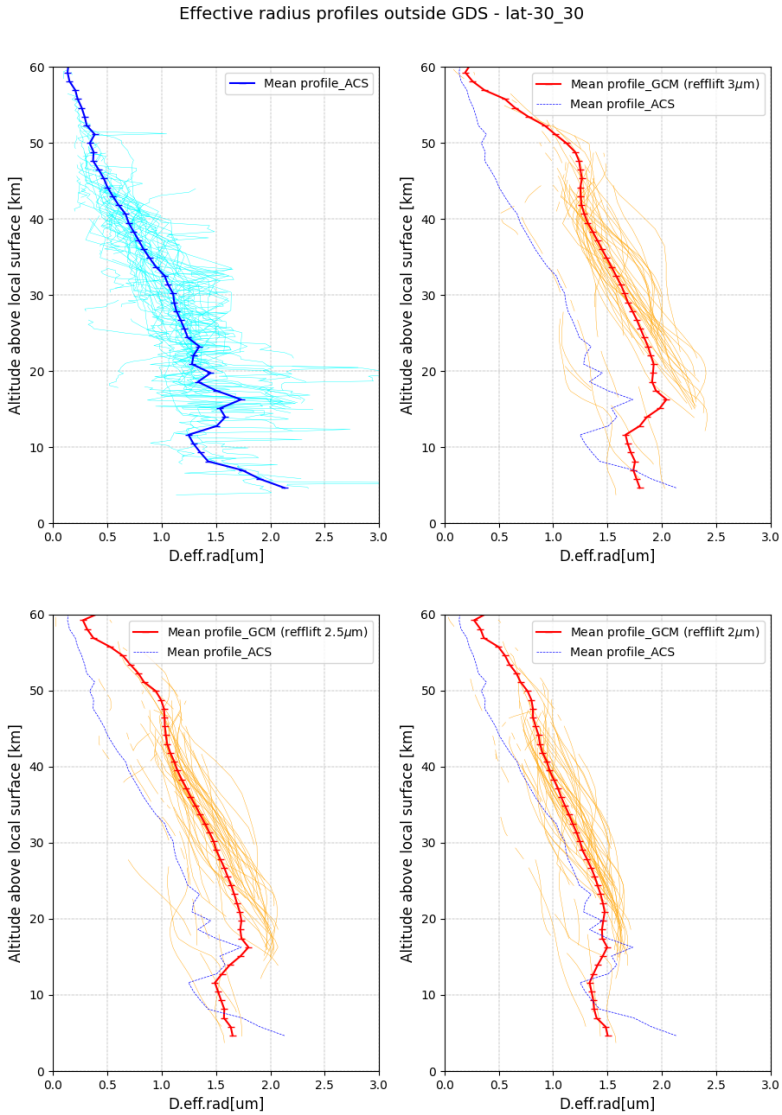

Figure 11: Effective radius occultation profiles, between latitude band of [30°S;30°N], Ls [170.2°;195°] (before GDS) and [240°;255.1°] (GDS decay phase). The average of all the profiles interpolated on a 100 levels vertical grid is displayed in blue for ACS and in red for the GCM. **Top,Left:** ACS (MY34) ; **Top,Right:** GCM with $r_{eff,lift}$=3µm (default) (MY29) ; **Bottom,Left:** GCM with $r_{eff,lift}$=2.5µm (MY29) ; **Bottom,Right:** GCM with $r_{eff,lift}$=2µm (MY29).

before, a 2-microns size at injection would not allow for such observed radii during the dusty season.

The effects of drifting the dust size distribution towards smaller particles can be seen on Figures 14 and 15, as the far IR opacity slightly decreases and gets closer to *MCS*, while the visible opacity rises a little. This implies a small increase in the atmospheric temperature, as the dust absorbs more the sun radiation.

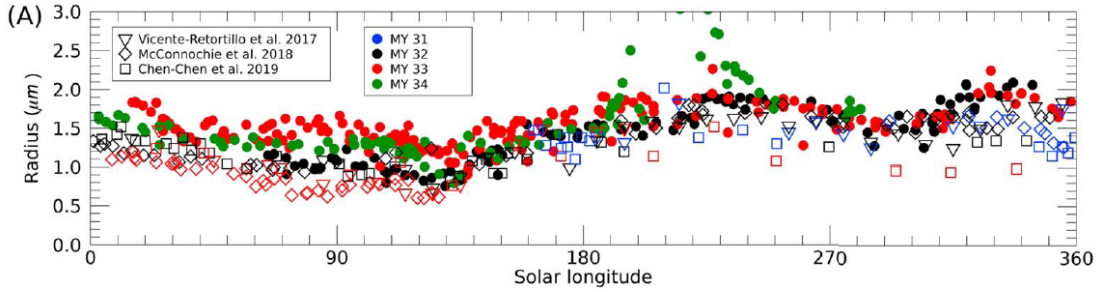

Figure 12: Figure 2.(A) from Lemmon et al. [2019]. Retrieved dust r_{eff} for MY 31 (blue), 32 (black), 33 (red), and 34 (green) is shown, according to different studies: circles, Lemmon et al. [2019]; triangles, Vicente-Retortillo et al. (2017); diamonds, McConnochie et al. (2018); and squares, Chen-Chen et al. (2019).

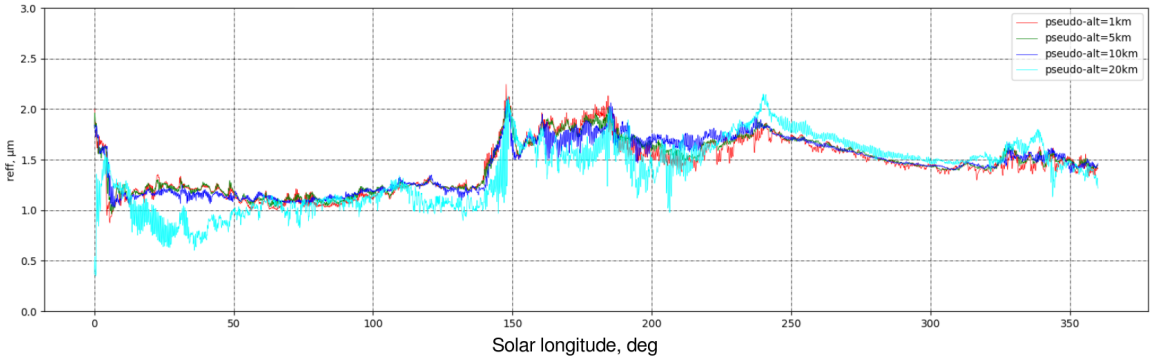

Figure 13: Evolution in Ls of the GCM effective radius interpolated above Curiosity's site, at different pseudo-altitudes : 1km (red), 5km (green), 10km (dark blue), 20km (cyan). The GCM simulation uses the dust scenario forcing of MY29, with $r_{eff,lift}$=2.5μm.

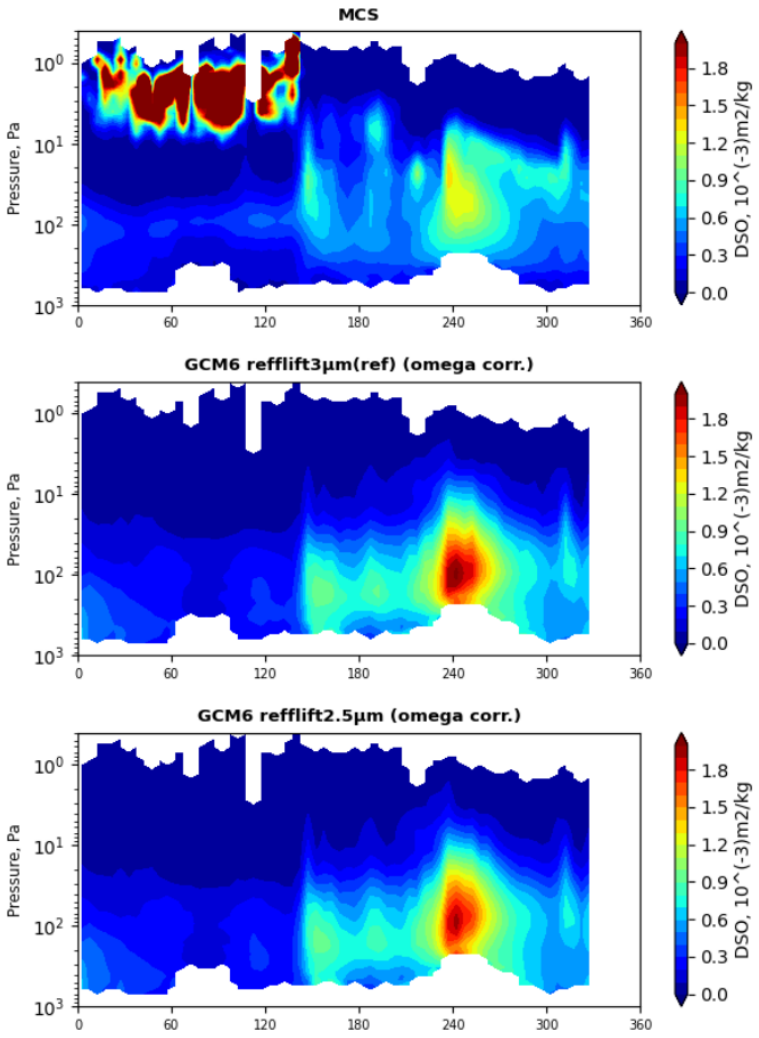

Figure 14: Nighttime dust Density-Scaled Opacity at 21.6µm from *MCS* and several GCM simulations - Zonal & meridional average in latitude band of [30°S;30°N] - MY29. **Top to bottom:** *MCS* ; GCM6, varying IR to VIS coef., $r_{eff,lift}$=3µm ; GCM6, varying IR to VIS coef., $r_{eff,lift}$=2.5µm.

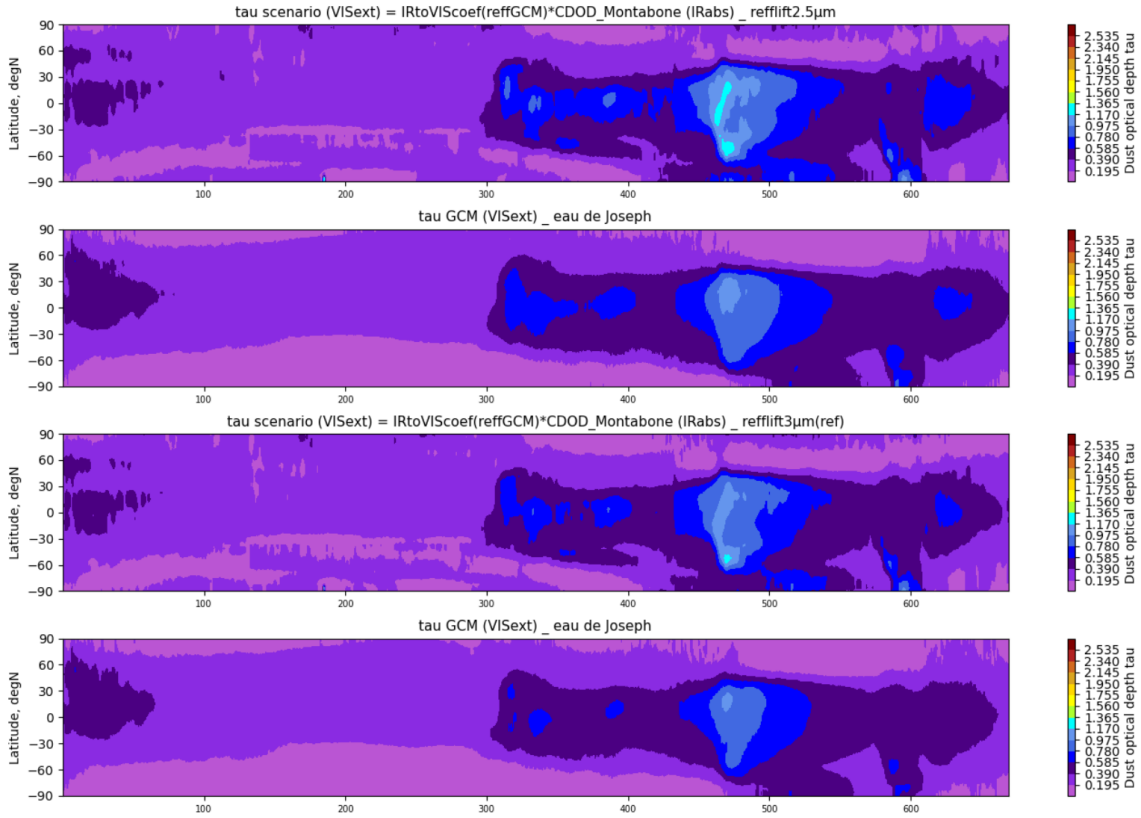

Figure 15: Time[sols]-latitude[°N] evolution maps over MY29 of visible $\tau_{scenario}$ and τ_{GCM} with different $r_{eff,lift}$. **Top 2 plots:** The visible CDOD scenario forcing, with varying IR to VIS coefficient and $r_{eff,lift}$=2.5µm, and the correspondingly driven visible CDOD from the GCM. **Bottom 2 plots:** same plots as above but with the former $r_{eff,lift}$=3µm. Every integrated optical depths are normalized to a pressure of 610Pa.

3 Injection timing

The previous reports already explored the sensitivity of the injection timing on the creation of *dust detached layers*. If narrow windows, like 8h-10h or 10h-12h, seemed more efficient at elevating dust via very concentrated *rocket dust storms*, according to *LMD_CNES_EXM_gcm6.0*, the report *LMD_CNES_EXM_2020_gcm_dust* showed that their effect was too strong comparing to *MCS* atmospheric dust amount, and that wider intervals like 10h-14h could dampen this effect while still maintaining some dust in mid-altitude.

However, since no clear physical justification arose for those restricted injection timings, we decided this year to widen again the lifting window, firstly to 8h-18h to follow the Planetary Boundary Layer average activation time, and finally to the full sol (0h-24h). Some studies like Chatain et al. [2021] also presented evidence for nighttime local turbulence near the surface, motivating us further to keep a dust lifting active at every local time of the sol (even though this turbulence and wind stress are not modeled in the GCM).

Technically, *storm dust* is still injected at night, as during daytime, but is very quickly detrained into background dust as no sunlight makes it ascending. The near-surface layers of the GCM fill up with dust, that can be entrained as soon as a true *rocket dust storm* forms in the morning.

4 Results and discussion

We gathered all the improvements mentioned above in one simulation of the Martian Year 29, with the following parameters :

- the varying conversion coefficient between the absorption 9.3µm CDOD and the visible extinction scenarios used in the GCM *(Section 2)* ;
- a dust injection distributed during the whole day (0h-24h) *(Section 3)*, with an injection coefficient C_{inj}=0.25 *(see previous report LMD_CNES_EXM_2020_gcm_dust)*, and an effective radius $r_{eff,lift}$=2.5µm for the lifted storm dust *(Section 2)* ;
- a detrainment coefficient C_{det} of 0.02 for the *rocket dust storms* *(see previous report LMD_CNES_EXM_2020_gcm_dust)* ;
- the revisited *mountain top flows* scheme, with 19 meshes activated and a mesh fraction $x_{mons} = 0.5\frac{h_{mons}-h_{min}}{h_{max}-h_{min}}$ *(Section 1)* ;
- some improvements in the water cycle done by Joseph Naar, which are not treated in this report.

We can then compare this new simulation to a GCM6 simulation with the full dust cycle (dust injection, *rocket dust storms*, old *mountain top flows* - see *LMD_CNES_EXM_2020_gcm_dust*) from January 2021, and to a GCM5.3 simulation.

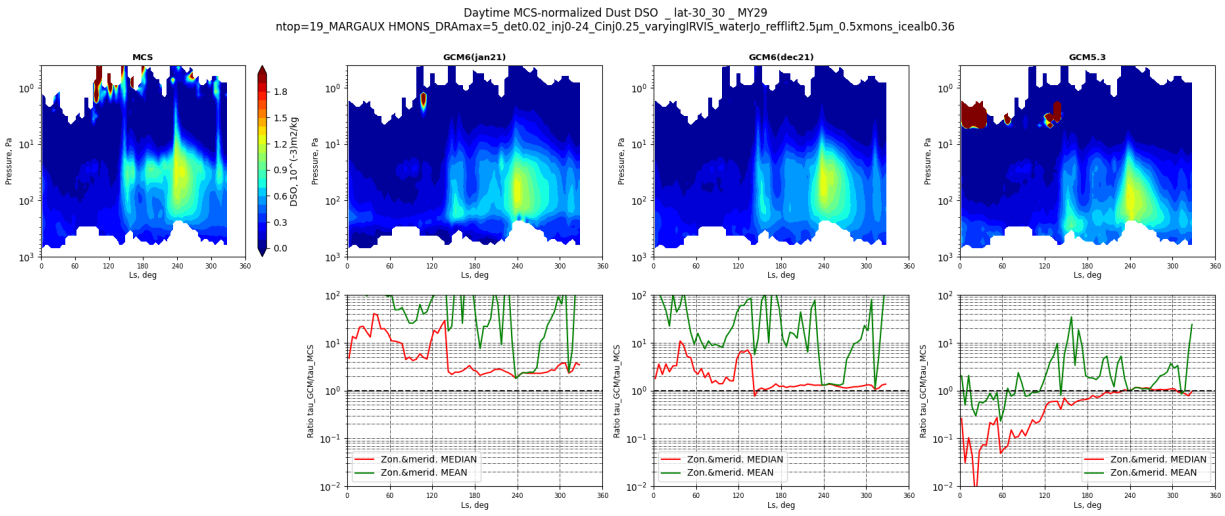

Figure 16: Daytime dust Density-Scaled Opacity at 21.6µm from *MCS* and several GCM simulations - Zonal & meridional average in latitude band of [30°S;30°N] - MY29. **Top raw, left to right:** *MCS* DSO ; *MCS*-normalized old GCM6 DSO ; *MCS*-normalized new GCM6 DSO ; *MCS*-normalized GCM5.3 DSO. **Bottom raw, left to right:** τ ratios between respectively old GCM6, new GCM6 and GCM5.3, to *MCS*. The red line represents the zonal & meridional median in the [30°S;30°N] band, while the green one stands for the average. The wide black dashed line emphasizes a ratio of unity.

Figures 16 and 17 illustrate the agreement of these simulations to the *MCS* opacity, in terms of profile shape on the one hand, and of absolute integrated optical depth on the other hand. Indeed, these figures' top raws present the GCM dust Density-Scaled Opacity

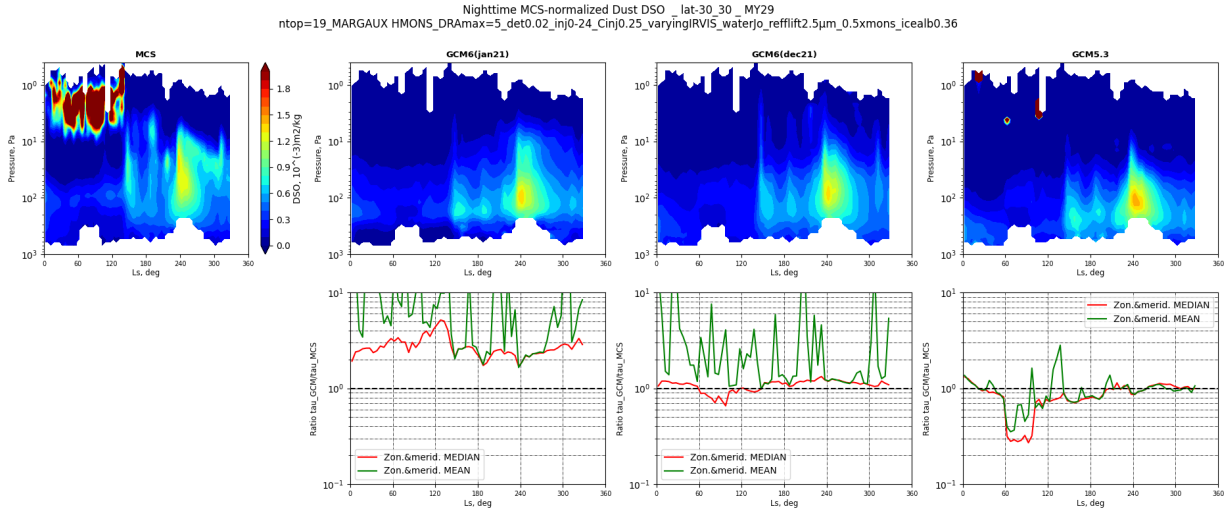

Figure 17: Same than Figure 16 for nighttime profiles.

profile normalized by the local column-integrated optical depth of the *MCS* binned profile. To do so, when the GCM data are processed through our *MCS* observer simulator (see *LMD_CNES_EXM_2020_gcm_dust*) and interpolated at *MCS* observations location, the simulator also computes locally the column-integrated optical depth of both *MCS* and interpolated GCM profiles, and outputs the ratio :

$$\tau\ ratio = \frac{\sum_{l=l_{MCS,bot}}^{l_{MCS,top}} [\partial_z \tau_{GCMinterp.}(l)\ \Delta P_{lev,MCS}(l)\ /\ g\rho_{MCS}(l)]}{\sum_{l=l_{MCS,bot}}^{l_{MCS,top}} [\partial_z \tau_{MCS}(l)\ \Delta P_{lev,MCS}(l)\ /\ g\rho_{MCS}(l)]} \tag{4}$$

with $P_{lev,MCS}(l)$ the mid-altitude pressure between two *MCS* pressure grid points $P_{lev,MCS}(l) = \sqrt{P_{MCS}(l-1)P_{MCS}(l)}$; and $\rho_{MCS}(l) = \frac{P_{MCS}(l)}{r_{atm} T_{MCS}(l)}$.

The dust vertical profile shape from the new GCM6 seems a good compromise between the older GCM6 very distinct *dust detached layers* and the GCM5.3 dust more confined near surface. We can notice two interesting features though. First, every GCM simulations, even the GCM5.3 one, exhibit this *detached layer*-like shape between Ls 60° and 100° once passed through the observer simulator and renormalized by *MCS* column. This could point toward an observational bias, especially as this shape disappears in the GCM5.3 simulation as soon as we look directly at the opacity profiles interpolated at 3am for instance (see Figure 18). Second, none of the GCM simulations achieve to get *detached layers* reaching as high as *MCS* ones.

Besides, considering the τ ratios, the median curves (red) indicate that our last simulation can lift satisfying amounts of dust at the levels comprised in *MCS* field of view. The mean ratios (green) of both GCM6 simulations are however far greater than unity and depict the presence of opacity profiles that are highly different from *MCS* in the considered dataset, underlining our difficulties to fully apprehend the complexity of the *MCS* observations and the phenomena they unveil.

On Figure 19 we examine the impacts the new dust cycle has on the mean atmospheric temperature.

During the clear season, although the dust cycle-related changes presented in this report do have an impact on the mid-altitude temperature (see for example Figure 10 in Section 2), the improvements in the water ice clouds representation, which are strong drivers of

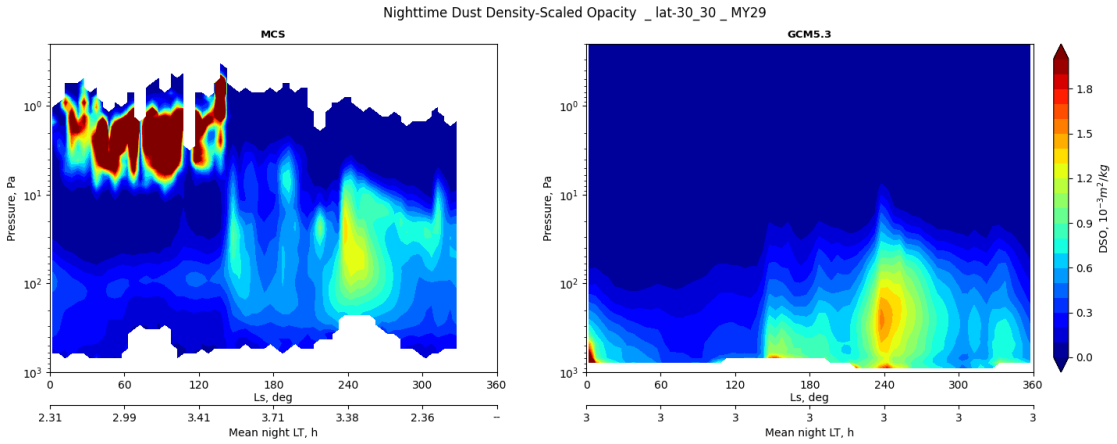

Figure 18: Nighttime dust Density-Scaled Opacity at 21.6µm from *MCS* (**left**) and GCM5.3 simulation just interpolated at 3am everywhere (**right**) - Zonal & meridional average in latitude band of [30°S;30°N] - MY29. Average local time of the *MCS* observation corresponding to the Ls labels is also written for comparison.

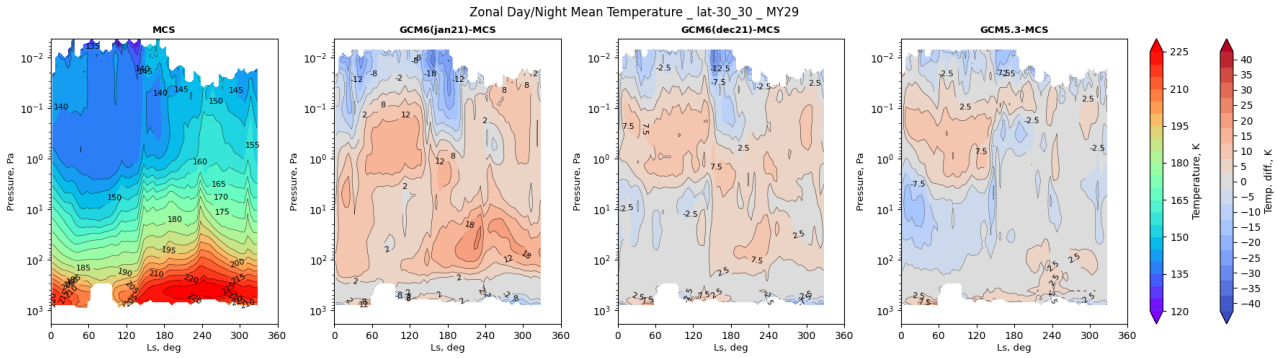

Figure 19: Diurnal mean temperature from *MCS* and GCM simulations - Zonal & meridional average in latitude band of [30°S;30°N] - MY29. **Left to right:** *MCS* absolute temperature ; Temperature difference between old GCM6 and *MCS* ; Temperature difference between new GCM6 and *MCS* ; Temperature difference between GCM5.3 and *MCS*.

the thermal structure at this time of the year, also explains our better results compared to GCM5.3. We can also note that the dust cycle has very little influence then on the high-altitude ($P < 2$Pa) temperature bias, which must be caused by another modeled process.

Later, the mid-altitude (200Pa-10Pa) hot bias of the dusty season is strongly diminished compared to the full dust cycle simulations of last year, but still present. The temperature in the lower layers ($P > 200$Pa) is slightly closer to observations than GCM5.3, whereas high altitude seems impacted by the presence of the aerosol particles. This persisting hot bias linked to the dust ascension could be resolved in future versions of the GCM by implementing the non-local thermal equilibrium between dust and gas above 40km, which has been brought in light by Goldenson et al. [2008] and recently tested in a 1-D radiative-convective model by Haberle et al. [2021].

Finally, we look at day-night temperature anomaly, as a proxy for the atmospheric ther-

mal tides generated by the sun insolation diurnal cycle. The new GCM6 simulation offers very convincing anomaly, even though the phasing of the tides is still a bit off, as illustrated on one month (Ls 210°-240°) in Figure 20.

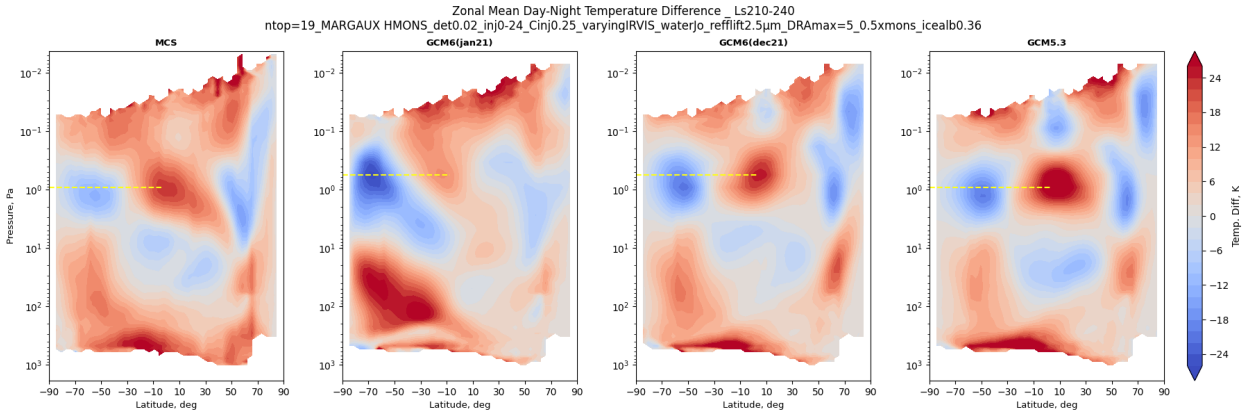

Figure 20: Diurnal mean temperature anomaly from *MCS* and GCM simulations - Zonal & temporal average between Ls 210° and 240° - MY29. **Left to right:** *MCS* ; old GCM6 ; new GCM6 ; GCM5.3. The yellow dashed line points at the local maximum of the anomaly, in order to better evaluate the waves phase.

Conclusion

The dust cycle is one of the main driver of the Martian climate. Its contribution to the radiative transfer, via absorbing the sun radiations and emitting in thermal infrared, affects the surface temperature, as well as the thermal structure of the atmosphere, and therefore the dynamics, at both local and global scales. Since particles serve as nucleii for the condensible species, namely water vapor and CO_2, the dust atmospheric distribution can also interact with the microphysics and impact the formation of clouds. It is thus essential to correctly characterize it in the model. This is especially true as the version 6 of the GCM aims to take a step toward a dust modelling that is more closely linked than before to physical processes, instead of mainly consisting in an external forcing. Previous studies, as presented in last years reports, indicated the LMD GCM6 dust cycle modelling required some corrections and improvements before we could integrate it in realistic simulations needed for the Mars Climate Database. This is what we focused on during this year 2021.

We began by correcting our *mountain top flows* parametrization that reinjected too much dust in the atmosphere and unrealistically took into account some slopes that should not present the dust concentrating and ascending effects we simulate. While we have not yet taken the opportunity to explore the new scheme locally around each 19 summits it features, their effect now appears at least reasonable at the global scale.

We were also able to partially solve a discrepancy that had appeared between the visible Column-integrated Dust Optical Depth scenarios and the *Mars Climate Sounder* dust infrared opacity profiles while "adding more physics" in the model, namely computing online the coefficient needed to convert the IR scenario into the visible GCM forcing. As this coefficient depends on the particle size distribution, this was the occasion to better constrain the GCM dust effective radius accordingly to other observational datasets, covering respectively the mid-altitude and the near-surface atmosphere. These changes toward a more realistic model also had the welcome effect of dampening the mid-altitude hot bias that exists in the GCM6 during the Southern summer.

Getting more realistic also means giving up on ideas when they don't seem to be robustly founded. This is why we decided to expand the injection timing from the small local time window of 10h-12h to the whole sol, night included, as not enough data supported such a preferential timing for the lifting of dust aerosols.

These changes resulted in numerous improvements on the dust distribution as well as the thermal structure, in regard to observations. Some persisting biases, like on the dusty season temperature, still give us room for progress in modelling correctly the dust contribution to the Martian climate. Nevertheless, we are now sufficiently satisfied to base the future production of the Mars Climate Database 6.1 on this configuration of the dust cycle, and apart from small fixes, we are now focusing on correctly tuning the water cycle.

References

Chatain, A., Spiga, A., Banfield, D., Forget, F., and Murdoch, N. (2021). Seasonal Variability of the Daytime and Nighttime Atmospheric Turbulence Experienced by InSight on Mars. *Geophys. Res. Lett.*, 48(22):e95453.

Goldenson, N., Desch, S., and Christensen, P. (2008). Non-equilibrium between dust and gas temperatures in the Mars atmosphere. *Geophys. Res. Lett.*, 35:8813–+.

Haberle, R. J., Kahre, M. A., Hartwick, V., Bertrand, T., Wilson, R. J., Wolff, M. J., and Batterson, C. (2021). Loss of thermal contact between dust and gas in the mars atmosphere. In *AGU Fall Meeting Abstracts*, volume 2021, pages P35F–2196.

Kleinböhl, A., Schofield, J. T., Abdou, W. A., Irwin, P. G. J., and de Kok, R. J. (2011). A single-scattering approximation for infrared radiative transfer in limb geometry in the Martian atmosphere. *Journal of Quantitative Spectroscopy and Radiative Transfer*, 112:1568–1580.

Kleinböhl, A., Schofield, J. T., Kass, D. M., Abdou, W. A., Backus, C. R., Sen, B., Shirley, J. H., Lawson, W. G., Richardson, M. I., Taylor, F. W., Teanby, N. A., and McCleese, D. J. (2009). Mars Climate Sounder limb profile retrieval of atmospheric temperature, pressure, and dust and water ice opacity. *Journal of Geophysical Research (Planets)*, 114:10006.

Law, E. and Day, B. (2017). Mars Trek: An Interactive Web Portal for Current and Future Missions to Mars. In *European Planetary Science Congress*, pages EPSC2017–99.

Lemmon, M. T., Guzewich, S. D., McConnochie, T., de Vicente-Retortillo, A., Martínez, G., Smith, M. D., Bell, J. F., Wellington, D., and Jacob, S. (2019). Large Dust Aerosol Sizes Seen During the 2018 Martian Global Dust Event by the Curiosity Rover. *Geophys. Res. Lett.*, 46(16):9448–9456.

Luginin, M., Fedorova, A., Ignatiev, N., Trokhimovskiy, A., Shakun, A., Grigoriev, A., Patrakeev, A., Montmessin, F., and Korablev, O. (2020). Properties of Water Ice and Dust Particles in the Atmosphere of Mars During the 2018 Global Dust Storm as Inferred From the Atmospheric Chemistry Suite. *Journal of Geophysical Research (Planets)*, 125(11):e06419.

Montabone, L., Forget, F., Millour, E., Wilson, R. J., Lewis, S. R., Cantor, B., Kass, D., Kleinböhl, A., Lemmon, M. T., Smith, M. D., and Wolff, M. J. (2015). Eight-year climatology of dust optical depth on Mars. *Icarus*, 251:65–95.

Montabone, L., Kass, D., Kleinboehl, A., McCleese, D., and Schofield, J. (2017). NetCDF version (v3.0) of MRO/MCS binned retrievals v5.2 of temperature and dust/water ice opacities. *Internet*.